Published in International Journal of Fatigue, *160*, [106852], 2022

Effect of heat treatment on fatigue crack growth in multiple material layered IN718/316L structure fabricated by laser powder bed fusion

M-S Duval-Chaneac[1, 2], N Gao[1], R.H.U Khan[3], M Giles[1], K Georgilas[2], X Zhao[1], P.A.S Reed[1]

[1] Materials Research Group, Faculty of Engineering and Physical Sciences, University of Southampton, Southampton, SO17 1BJ, UK

[2] NSIRC, TWI Ltd., Granta Park, Great Abington, Cambridge, CB21 6AL, UK

[3] TWI Ltd., Granta Park, Great Abington, Cambridge, CB21 6AL, UK

E-mail: marie-salome.duval-chaneac@affilliate.twi.co.uk or m-s.d.duval-chaneac@soton.ac.uk

Abstract

Multi-material specimens have been produced in layered architectures by Laser Powder Bed Fusion (L-PBF) process, combining 316L stainless steel to IN718 in a single operation. Specimen were then thermally post treated to reach the mechanical performances expected for IN718 via precipitation strengthening. A specific heat treatment has been tailored for the combination of 316L and IN718 multi-layered specimen, and has been investigated in regards to its effect on the mechanisms of crack propagation. This work aims to control the near tip crack driving force by the combined effect of microstructure strengthening and the shielding effect multiple-layer architecture to mitigate crack propagation.

Key words

Multi-materials, additive manufacturing (AM), Interface, Heat treatment, Crack growth rate

1. Introduction

2. Materials and Methods

Both 316L and IN718 alloy powders were gas atomised by Sandvik Osprey producing spherical metallic powder particles in the size range of 20-50 µm. The powder size was measured using Malvern Morphologi 4 automated microscope, flowability was measured by the Hall Flowmeter funnel (measuring the flow time for 50g of powder), and tap density was measured for 3000 taps, according to the ASTM B213 standards [32]. The chemical composition of the powder was measured by external contractor AMG analytical (UK) by Inductively Coupled Plasma (ICP), and for lighter elements such as Carbon and Oxygen, contents were measured by thermal infrared and inert gas fusion respectively (LECO).

The L-PBF process was conducted using a HUAKE PM250 machine under an argon gas protective atmosphere, using the parameters shown in Table 1. The scanning strategy chosen was island scanning with a size of 5mm, and the scanning direction of each layer was alternated through a 90° angle. The ratio of process parameters, also named as the energy density ratio ($E_{dv,}$ see in $E_{dv} = P⁄h \times t \times v⁄ \ [J/mm^3]$), is often used for process parameter optimisation:

$$E_{dv} = \frac{P}{h \times t \times v} \ [J/mm^3] \quad (1)$$

where *P* is the power, *h* the hatch spacing, *t* the thickness of the powder layer displayed and *v* the scanning speed [33]. The energy density ratio employed for both materials was $E_{dv} = 140 \ J/mm^3$, which is within the optimal range of process parameters for high densification of each material according to studies on process parameter optimisation [34][35].

Table 1: L-PBF Process parameters used in this study for both 316L and IN718

Laser Power	Scanning speed	Hatch space	Layer thickness	Layer rotation
300W	900mm/s	0.08mm	0.03mm	90°

Bend bar specimens for fatigue testing were manufactured with dimensions of 10x10x60 mm, with IN718 as the top layer and 316L as the bottom layer (10x5x60 mm dimensions for each layer, as shown in **Error! Reference source not found.**). Six tensile rods of Ø10x60 mm dimensions were manufactured respectively for IN718 and 316L to test the tensile properties of each alloy separately. In order to assure consistency of grain orientation in the bending and tensile specimen, all the specimens were produced with their main longitudinal axis parallel to the building plate plane (**Error! Reference source not found.**).

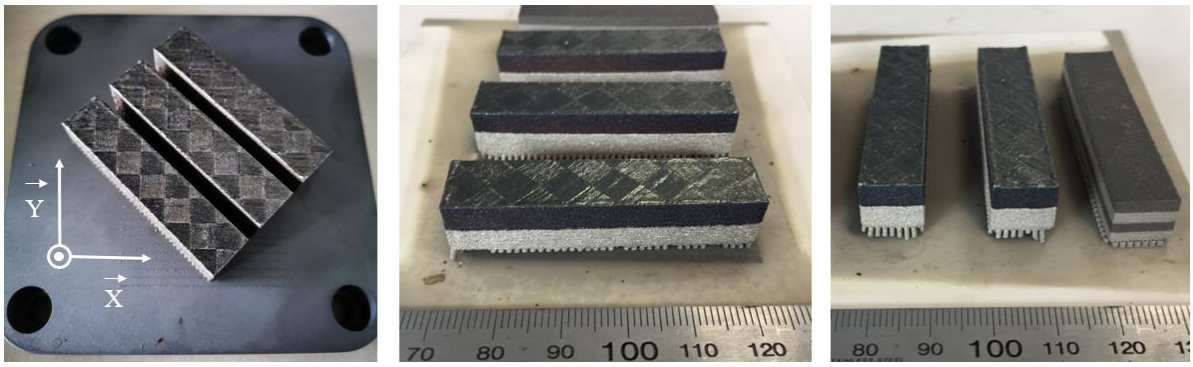

(a) (b) (c)

Figure 1 a) bi-layer bending specimen on building plate after heat treatment, b) side view of bi-layer specimen, c) front view including the 4-layer specimen

For metallographic analysis, bend bars were cut orthogonally to the longitudinal direction, then mounted in conductive Bakelite. Top surfaces of the specimens were mechanically ground using 800 and 1200 silicon carbide (SiC) grit papers before polishing using 6 µm, 3 µm , 1µm and 0.25 µm diamond finish. Etching was performed with: H_2O: HCl: H_2O_2 solution in 4:2:1 proportions. Porosity and microstructural observations were made using an Olympus BX-51 optical microscope (OM). ImageJ software was used on multiple micrographs, to quantify the porosity content of each specimen. For each specimen, six micrographs were taken providing a total area of study of 54.6mm². Scanning electron microscope (SEM) and X-ray spectroscopy (EDS) analysis were conducted by JEOL-JSM 5910 under 15-20kV for SEI imaging, at a typical working distance between 8.5 to 10mm. Backscatter electron (BSE) imaging and electron back scatter diffraction (EBSD) analysis were conducted using 20kV and a 120 µm aperture, a step size of 0.57µm and Channel5-HKL software. The observations were conducted along the build orientation of the specimen (z direction), then analysed by using Aztec software for grain size, shape and orientation. Macro-observation of specimen fracture surfaces was carried out using an Alicona G4 Infinite Focus, to allow roughness imaging for the fracture surfaces.

Vickers micro-hardness (HV) tests were conducted in accordance with BS EN ISO 6507 [36]. Hardness was measured using 300gf with dwell time of 15s. Measurements were made on cross sections of the specimens (10mm of edge length), with 50µm distance between each indentations. Nano-indentation measurements were taken across the interface to assess the hardness and modulus changes, 50 indent rows offset by 30 µm were made, with 5 indents per row spaced by 10 µm each, for a total length of measurement covering 1500 µm across the interface region (750 µm in the Inconel layer and 750 µm in the 316L layer). Measurements were done in depth control until 300 nm depth, indentation speed was set at 7mN/s.

Tensile tests were carried out for each alloy separately at room temperature by an external contractor, Westmoreland mechanical testing (UK), in accordance with the ASTM E8 standard at room temperature [37]. Specimens were manufactured out of the AB tensile rods, horizontally built with respect to the building plate (i.e. the main rod axis is within the X-Y plane of the building plate), see Figure 2. An extensometer was used for the first part of the test

at a strain rate of $0.005.min^{-1}$, then switching to cross head displacement at a strain rate of $0.05.min^{-1}$ for a faster displacement rate until final failure.

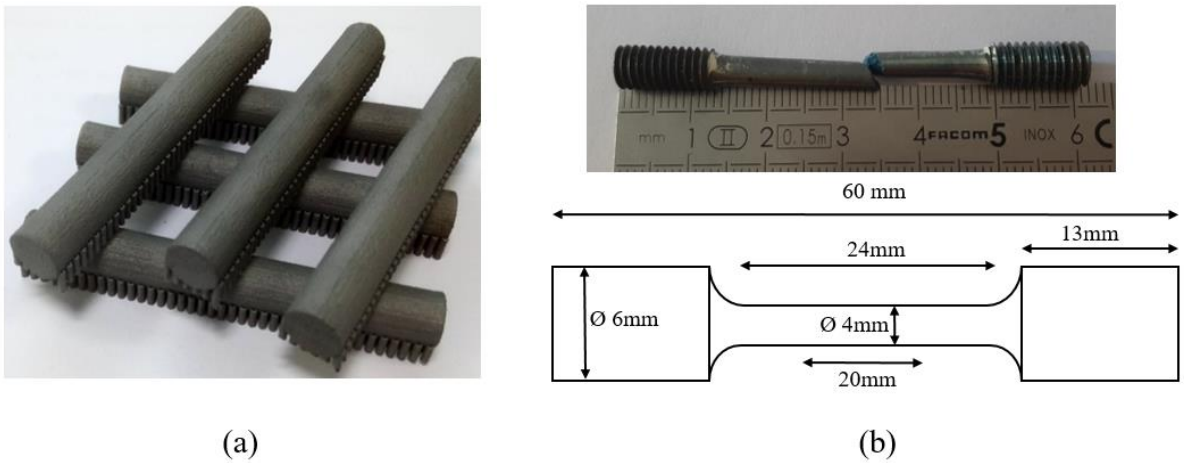

Figure 2 a) Tensile rods were manufactured for each alloy separately, b) Dimensions of tensile specimen after manufacturing from the AB rods for testing according to ASTM E8 standard

Long crack tests were performed under three-point bending, on an Instron 8502 servohydraulic machine, with sinusoidal loading at R = 0.1, and frequency f=10Hz. The bend bars were notched in the centre using wire cutting to produce single edge notched bend (SENB) samples as shown in Figure 3. The depth of the notch is 1.25mm, corresponding to 1/4 of the depth of the layer (or 1/8 of the total depth of the bend bar). The pre-cracking was carried out by load shedding from an initial ΔK (of 15 MPa√m), then successively stepped down by 10% increments, after the crack grew through 4 monotonic plastic zone sizes at a given ΔK-level (down to a ΔK of 10.4 MPa√m for 316L and 12.6 MPa√m for IN718). Subsequent crack growth tests were conducted following the BS EN ISO 12108:2012 standard [38] under constant load, increasing ΔK-conditions. One test was performed under constant ΔK-conditions, by altering the loading condition as the crack advanced to keep ΔK within 10% of the original value, in order to determine the crack propagation rate base line within each layer for a given crack tip stress intensity factor (results are displayed in section **Error! Reference source not found.**). The top surface of the specimens was ground using 120, 800, 1200 SiC grit paper and then polished using 6 µm, 3 µm, 1 µm diamond suspension. Crack length was monitored by a direct current potential drop (DCPD) method. Two probes were welded on the top surface on each side of the initial notch (denoted as X values) and the other two probes (denoted as Y) were welded on the lateral side (away from the center) to measure the base line potential of the current flow in the specimen. The fatigue crack growth rates da/dN were then derived from the curve of the variation in the electrical potential with time, translated to an empirically determined crack length *a* versus *N* relationship, and *da/dN* determined by the secant method. A standard calibration using tin foil was carried out to ensure the correct V/V_o to *a/W* relationship for the DCPD device. This technique was employed because the resistivity of both alloys were considered similar in regards to the specimen dimensions: 7.400E-07 Ohm-m for 316L and 1.250E-06 Ohm-m for IN718, hence effects on the calculation of crack length were considered negligible, this was also checked by post-test crack length measurements.

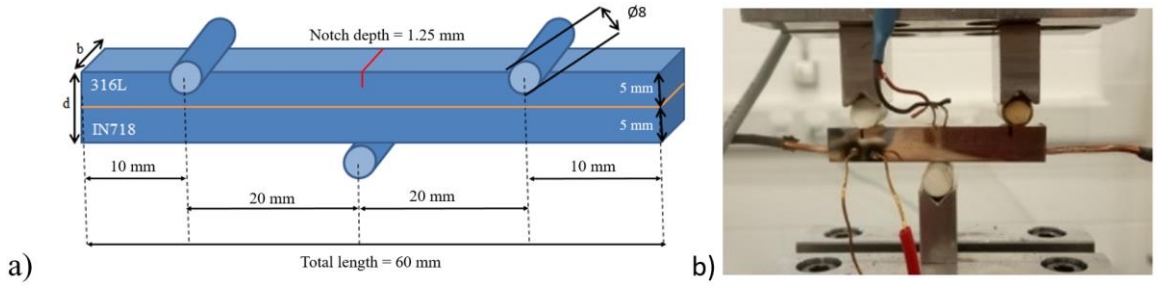

Figure 3: a) Schematic of notched bend bars under 3 point bending, b) Image of specimen

The heat treatment performed was: annealing at 1050°C / 45 min, followed by argon gas quenching, then ageing at 620°C /8hours followed by air cooling, and was performed in a vacuum brazing furnace from M&G Engineering using argon gas quenching after annealing.

AMS2759 for 316L stainless steel recommend annealing at 1060°C followed by air or vacuum gas quench [39]. AMS5662 and AMS5383 for IN718 recommend a first annealing stage followed by a double stage ageing treatment (720°C/8h FC to 620°/8h AC to RT) [40], [41].

Temperatures above 1032°C are considered elevated enough to support promoting the release of Nb in the IN718 matrix. Ageing time has been chosen to reduce the temperature exposure to 8 hours instead of the 18 hours (recommended by standards for IN718, [40][41]), hence the full precipitation strengthening from secondary phase γ' and γ" won't be fully achieved. The optimal coarsening and bi modal distributions of the secondary strengthening phases within IN718 won't be fully reached. However, the ageing time temperature was chosen, to minimize the formation of detrimental phases such as: σ phase within 316L, and δ orthorhombic phase that is a derived for of γ" Ni_3Nb . Sigma (σ) phase formation in 316L has a low kinetics of formation (i.e. it is sluggish) and requires an extended exposure within the temperature range 600-800°C [27], similarly for delta (δ) phase formation in nickel base alloy with a high chromium content, both of which can potentially reduce the ductility and toughness.

3. Results & Discussion

3.1. Characterisation of the metallic powders

The physical properties of the powders are displayed in Table 2 and the analysis of the elemental composition is displayed in

Table 3.

The 316L powder used in this study has more satellites and some agglomerations of powder are creating a larger mean diameter, but are also forming a more compact tap density by allowing interstitial powder stacking, which reduces the risk of creating porosities during the fabrication process. The chemical composition of 316L powder shows a long list of minimal elemental additions however, these concentrations remain very low. Similarly, the main chemical composition of IN718 powder falls within the range of the standard alloy composition except with some minor elemental traces. However, it is important to note the presence of N in the composition of 316L. N solute atoms can lower the stacking fault energy of 316L SS and have an effect on deformation twinning, contributing to the high tensile ductility of AB L-PBF 316L [42].

Table 2: Physical powder properties

	316L	IN718
Powder diameter size	28.2±12 µm	22.5±7 µm
Tap density	5.4 g/cm³	6 g/cm³
Flow ability	15 ±0.3 g/s	11.6±0.1 g/s

Table 3 : Chemical composition of IN718 and 316L powders used in this study, and comparison with standard material

Element (wt%)	316L Powder	IN718 Powder	Standard wrought 316L[43]	Standard wrought IN718[44]
Ni	12.29	52.46	10 - 14	50 - 55
Cr	17.34	18.71	16 - 18	17 - 21
Fe	64.95	19.57	Bal.	Bal.
Nb	0.04	4.8	-	4.75 - 5.5
Mo	2.49	2.93	2-3	2.8 - 3.3
Ti	<0.02	0.69	-	0.65 - 1.15
Al	<0.02	0.36	-	0.2 - 0.8
Cu	0.17	0.02	-	0.3 max
C	0.02	0.02	0.03	0.08 max
Co	0.08	0.09	-	1 max
Mn	1.49	0.04	2	0.35 max
Si	0.85	0.09	0.75	0.35 max
B	<0.02	<0.02	-	0.006 max
N	0.083	0.081	-	-

3.2. Characterisation of the microstructure

Figure 4 shows a backscattered image of a polished and etched specimen, the bi-layer specimen was built with IN718 as top layer and 316L SS as the bottom layer than heat treated, a diffusion zone is visible at the interface which also include some ductility dip cracking pointed by a red arrow. After heat treatment of IN718/316L specimen, the directional microstructure formed by the rapid cooling of the L-PBF process has not been erased but a change in microstructure is visible at the interface, where a diffusion zone of ~140µm width was measured. Within this diffusion zone some ductility dip cracking have been observed.

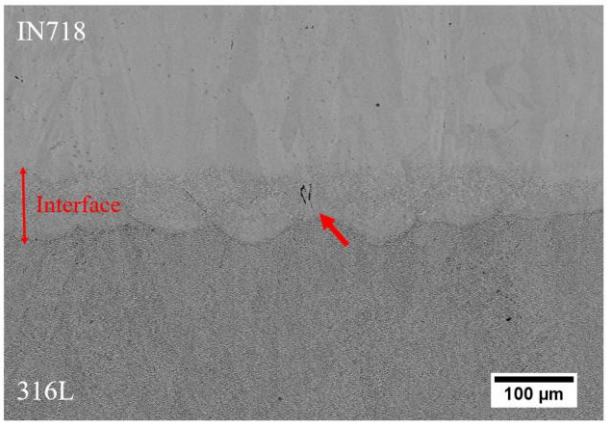

Figure 4 BSE image of the interface of heat treated specimen

The HTed microstructure of the IN718/316L specimen shown in Figure 5, reveals at larger magnification (in view 1, 2 and 3) the different changes in the sub-cellular microstructure. The sub-cellular structure within the 316L layer has evolved from a previous equiaxed structure of elongated sub-cells in the AB condition to a rounder (or hexagonal) homogenisation of the subcells within 316L grains. On the other hand the microstructure within IN718 layer is showing a dissolution of the sub-cellular structure and a migration of elements forming secondary phases both present in fine homogeneous precipitation within the grains, and in coarser amount at grain boundaries. A gradation in the amount of secondary phase precipitation at the grain boundary is also visible. The magnifies view 2 and 3 from Figure 5 shows that the closer to the interface the increased the amount of secondary phases present in the grain boundary area within the IN718 layer and the farther away from the interface the lesser the amount of coarse secondary phase in the grain boundary area is visible. However the formation of δ phase seems to have been successfully avoided, as no needle-like precipitates were observed.

Figure 6 shows an EDX map of the magnified image 2 from Figure 5, that is a view of IN718 layer area close the interface. It can be seen that Iron Chromium and Nickel elements are homogeneously distributed across the view forming the main γ matrix, but Niobium and Molybdenum are heavily segregated at the grain boundary forming a secondary phase most likely to be a Laves phase, and another secondary phase is also observed within the main γ matrix where Aluminium and Titanium are segregated most probably forming a γ’ phase, of

spherical shape and diameter of about 1.7µm. Some fine particles are also visible evenly distributed within the grain and seems to be holding Niobium and Molybdenum that would be coherent with a fine distribution of γ''.

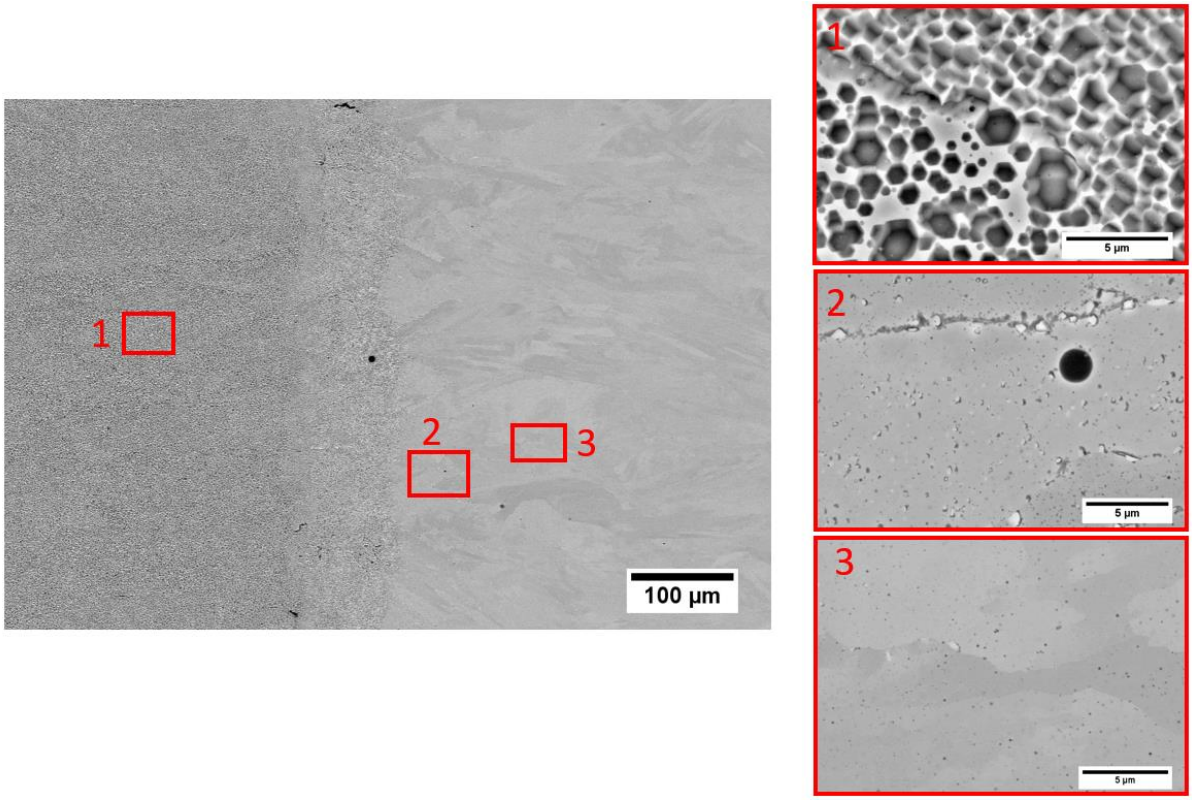

Figure 5 BSE of the interface of Heat Treated specimen with increase magnification in 1) 316L region, 2) IN718 region close to the interface and 3) IN718 farther from the interface region

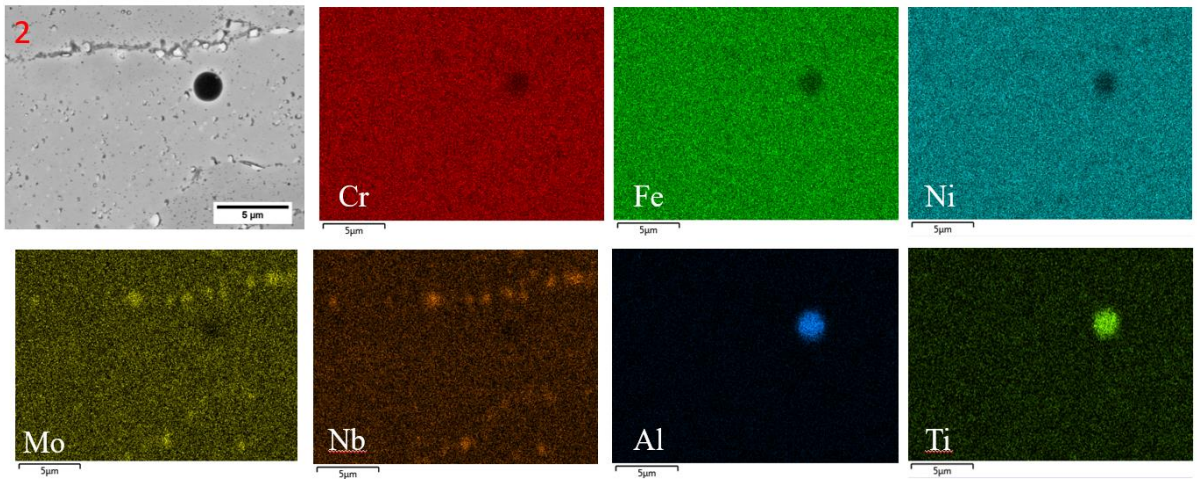

Figure 6 EDX map of the BSE image number 2 from Figure 5

Figure 7 shows an EDS linescan comparison between the elemental concentration distribution across the dissimilar interface in the AB state (Figure 7 a) and in HTed state (Figure 7b). The elemental diffusion is clearly apparent in the HTed specimen, where Iron and Nickel elements are displaying are following a steady slope over a band of ~140µm width (this distance represents 4 to 5 layers of the specimen build), than around the 600µm mark in the distance

axis (x axis) are displaying a jump in concentration just after a small steady step. This type of 'step' in elemental concentration is characteristic of the presence of an intermetallic phase formation [45].

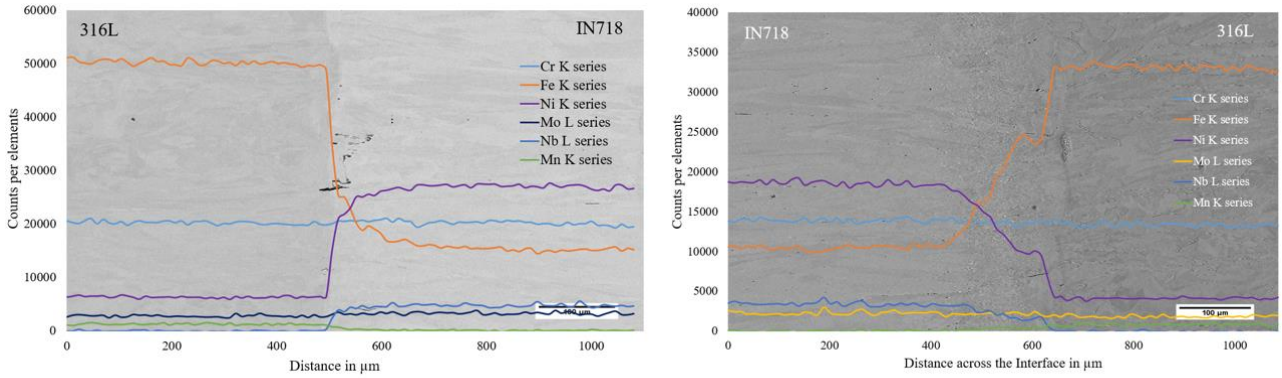

Figure 7 EDS linescan analysis of the interface region in a) AB specimen, b) HTed specimen

This observation is further supported by the BSE view of this area display in Figure 8, where a large number of secondary phases can be observed throughout the microstructure, in finer precipitates within the sub-cellular grains structure and in coarser form at grain boundaries and within the ductility dip cracking (DDC) sites. DDC is a solid state grain boundary embrittlement phenomenon, which occurs within a specific temperature range from 0.6 to 0.8 times the solidus temperature (Ts ~$[756-1100]°C$) where secondary phase precipitation and carbide formation at the grain boundaries, can prevent grain boundary gliding and may further cause the formation of voids and small cracks along grain boundaries [46]. The apparition of these DDC are supposed to take place during the annealing stage of the heat treatment, whereas as-built specimen were showing presence of rounder and smaller liquation cracking (also referred to as "hot" cracking and occur at higher temperature than DDC, see previously published paper?) [47].

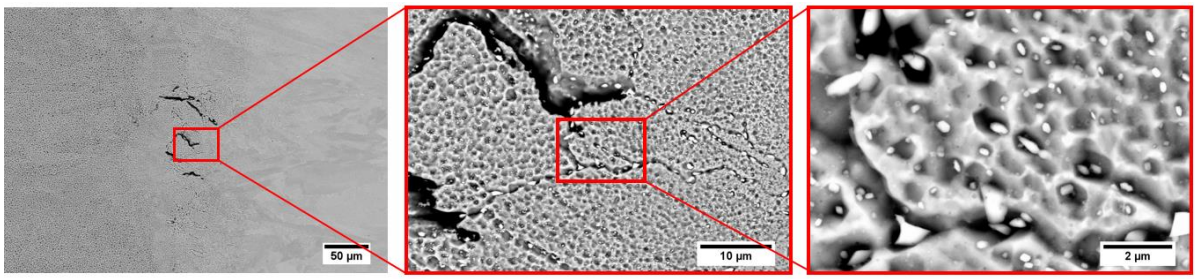

Figure 8 BSE of ductility dip cracking and secondary phases formation in the interdiffusion zone at the interface in HTed specimen

The existing presence of elemental segregation of the heavier refractory elements, such as Nb and Mo, in areas surrounding the sub-cellular structure within as-built L-PBF IN718 microstructure has been widely discussed in the literature [5]. This pre-existing elemental distribution across the primary microstructural features (specific of L-PBF process such as the

cellular/dendritic structure formed on solidification) will strongly affect the phase formation, and in turn also impact the solute element re-distribution during post treatment [48][18].

Elements with similar atomic radii tend to exhibit good solubility, typically the solubility of Iron in Nickel (at 1000°C) is 17 times superior to the solubility of Niobium in Iron, and 3 times superior to the solubility of Molybdenum in Iron (at the same temperature), meaning that during the annealing treatment, certain elements such as Iron have diffused across the interface creating an interdiffusion zone [49].

This diffusion of Iron will further affect the phase formation in the diffusion zone during the thermal post treatment of the multi-material specimen. The concentration in iron exerts a strong influence by affecting the segregation potential of Nb (variation of k_{Nb} as a function of nominal Fe content: i.e. Decrease in k value of Nb with increase in concentration of Fe). There is also a difference in various alloying elements' solubility between the mostly FCC Fe structure (316L layer) and the mostly FCC Ni structure (in IN718 layer). For comparison, differences in solid solubility of solute atoms are quoted as: in FCC Fe austenite can only dissolve 3wt% Mo, while FCC Ni austenite can dissolve 28wt% Mo, similarly Nb has 1.5wt% solubility in Fe and 18wt% solubility in Ni. Therefore the increase in Iron concentration in the diffusion zone leads to a decrease in Nb solubility in the γ matrix, and a similar trend is also observed for Mo [46].

The enrichment ratio is defined as the concentration of an element in the Laves phase over that in the bulk alloy. The elements Ni, Cr, and Fe do not strongly partition into Laves phases, while refractory elements such as Nb and Mo, partition rather strongly. In fact, it is now well known that Laves phase formation in Nb-bearing superalloy requires the presence of Nb to transform L→γ+Nbc (first to occur at 1250°C in IN718) and L→γ+Laves (second to occur at 1200°C in IN718) eutectic transformation. Formation of intermetallic phases such as Laves formation in the interdiffusion area at the dissimilar material interface is the cause of DDC and local embrittlement. The presence of intermetallic also causes void formation and decohesion with the matrix under HCF loading.

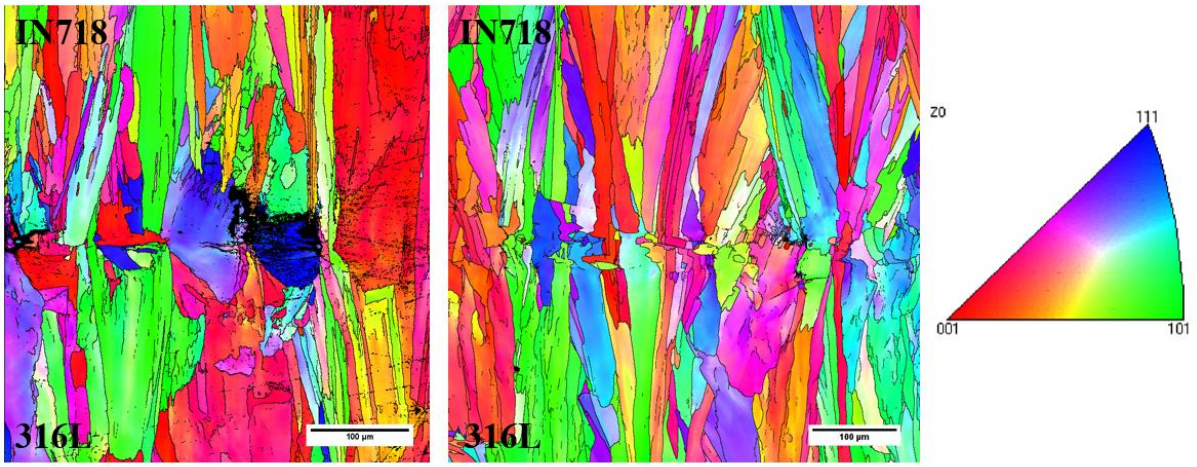

Figure 9 EBSD grain orientation map at the interface in a) AB and b) HTed

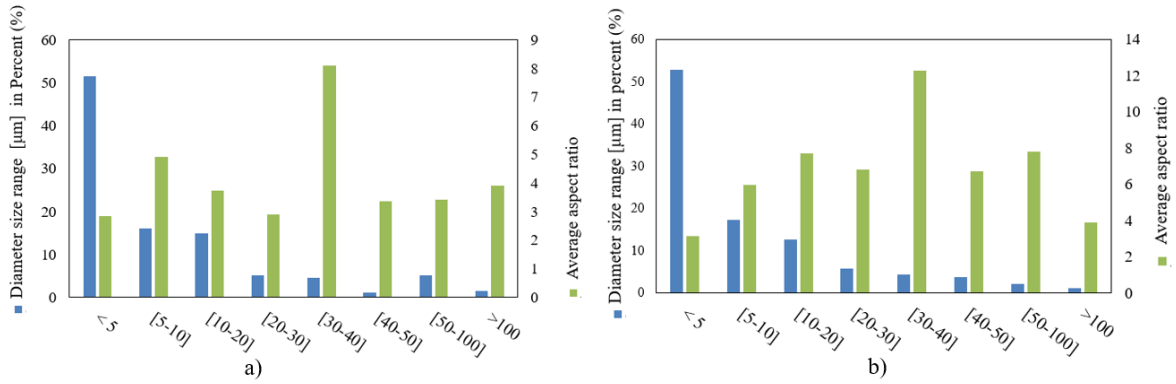

Figure 10 Grains size range distribution in percentage and aspect ratio in AB state a) 316L region b) IN718 region

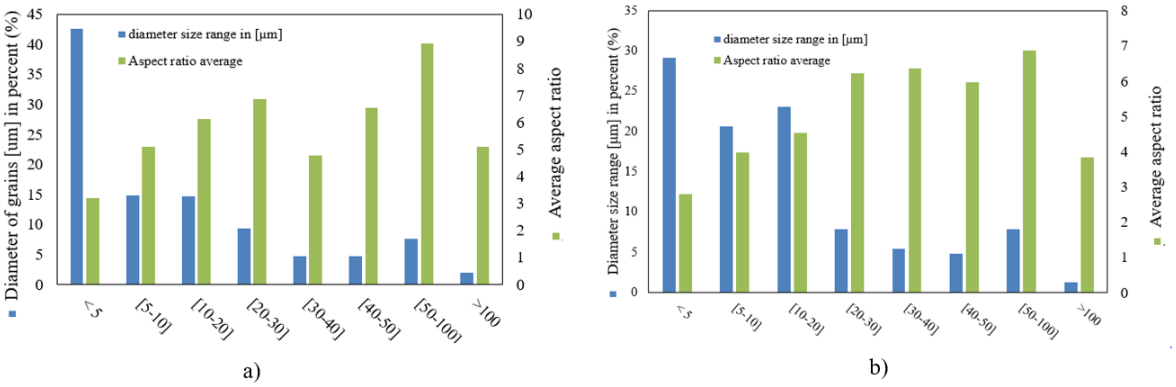

Figure 11 Grains size range distribution in percentage and aspect ratio in HTed state a) 316L region b) IN718 region

Modification of the grain structure was observed via EBSD and a comparison of the grain orientation map around the interface area is displayed in Figure 9. The comparison between the grain size distribution and the grain aspect ratio over the 316L and IN718 region is displayed in graphs Figure 10 for the AB specimen and in Figure 11 for the HTed specimen. Some smaller grains can be observed in Figure 9 b) at the interface in the HTed specimen. It is believed that the exposure to elevated temperatures during the annealing treatment (45 min at 1050°C), has led to some solid-state recrystallization and possible grain growth. In both IN718 and 316L, smaller grains tend to be rounder than large grains (30-40µm diameter), over 50% of the total grains are below 5µm diameter for both alloy systems in the as-built (AB) state. However, both alloys have undergone a degree of grain growth during annealing, reducing the total number of very small grains within the microstructure post thermal treatment.

3.3. Hardness and tensile properties

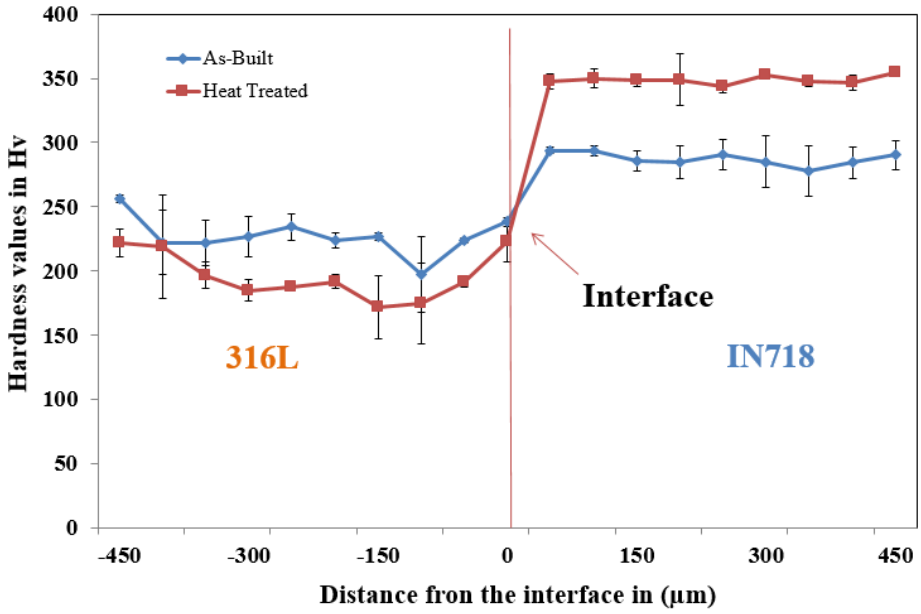

Figure 12 Vickers Micro-Hardness values measure across the interface comparison between AB and HT specimen

A series of micro-hardness measures was performed across the interface of bi-layer specimen in both AB and HTed state, and is displayed in Figure 12. Specimen under both condition display a gradual transition of properties.
It can be seen that the Vickers hardness for the IN718 has increased of 100 Hv after the heat treatment, while on the other hand the hardness of the 316L layer has dropped of about 50Hv after heat treatment. These measures can be explained by a thermally induced recovery from the former dislocations network that was surround the sub-cellular structure, and hence reducing the hardness in the 316L layer. On the other hand the IN718 layer has precipitated hard secondary phases, such as the strengthening γ' and γ'' phases, along with the brittle Laves phases increasing its hardness.

Table 4: Mechanical properties of each material from tensile tests and * nanohardness test

	Reduced Modulus (GPa)*	σ_y (MPa)	σ_u (MPa)	Elongation (%)	Hardness (GPa)*
AB 316L	156 ± 2	588 ± 2	709 ± 3	34 ± 2	2.1 ±0.04
AB IN718	165 ± 2	677 ± 11	784 ± 55	6 ± 2.2	2.7 ±0.3
HT 316L	141 ± 56	406 ± 0.8	672 ±1.7	36 ± 4	2.1 ± 1.14
HT IN718	160 ± 52	751 ± 7.8	957 ± 53	12 ± 2.6	3.6 ± 1.3

Table 4 show the results of the measures on the nano-indentation performed across the interface of both AB and HTed specimen along with the results of the tensile tests and their respective standard deviations. While the reduced modulus remain in a range consistent with the main FCC crystal structure of the γ matrix, the hardness show an increase in the IN718 layer post thermal treatment which is coherent with the micro-hardness measures.

The results of the tensile tests are also displayed in Figure 13 for a clearer comparison of the effect of the thermal treatment on the behaviour of each alloy. It can be seen that the heat treatment has had a positive impact on the IN718, 11% in YS(0.2%) from its AB condition, a noticeable 22% increase of its UTS and 50% increase in Elongation. However the results for the 316L have demonstrated a loss in YS of about 31% from its AB state, also a decrease in UTS of 5.2%, and a slight increase of 5.8% Elongation.

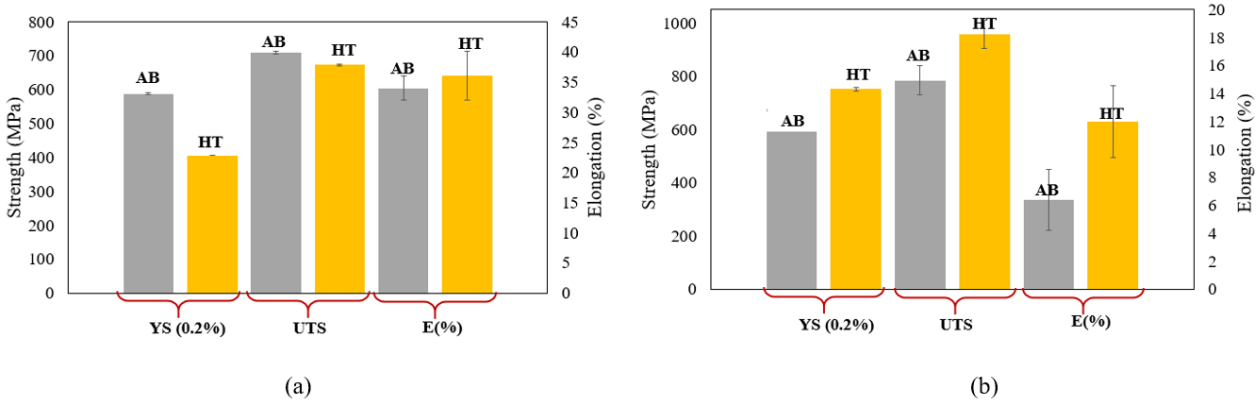

Figure 13 Tensile properties of a) 316L before and after HT b) IN718 before and after HT

Comparatively, L-PBF 316L processed for the bi-material specimen exhibits better hardness and mechanical properties, in AB condition rather than after HT. That is supposed to be due to the difference in dislocation density within the microstructure that is reduced by recovery during the exposure at elevated temperature during annealing treatment.
The Reduced Modulus and Hardness values of IN718 manufactured by L-PBF found in the literature tend to be around 180-200GPa and 6-7GPa respectively [50][51], which is higher than what was found by nano-indentation measures around the interface area.

3.4. Fatigue testing

3.4.1 Bilayer specimen

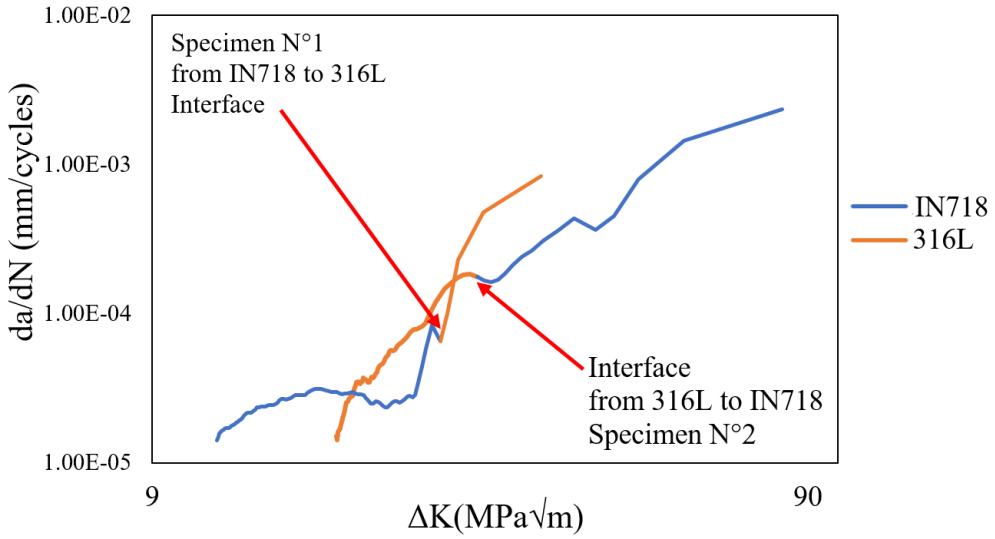

Figure 14 Long crack test, increasing ΔK propagation test in HTed specimen: Bilayer propagation from 316L to IN718 (specimen N°2) and from IN718 to 316L (specimen N°1)

The crack propagation within the specimen N°1, started at a ΔK of 10MPa√m and display a slow propagation within the first IN718 layer almost a stable propagation rate until the crack tip gets close to the interface where a rapid increase in propagation rate is observed leading to a rapid fatal failure within the 316L bottom layer (see Figure 14). It can be seen in Figure 15 b) a view of the roughness map of the final fracture surface of specimen N°1, which shows the presence of a ductile dimples within the 316L bottom layer characteristic of a fast final failure. Hence it can be said that the rate of crack propagation has been successfully diminished within the IN718 layer but when the propagation reached the anti-shielding transition (from hard to soft) the crack propagation rate has increase dramatically leading to accelerated fast failure in ductile fashion within the 316L layer.

The crack propagation within the specimen N°2 (see Figure 14), started at a ΔK of 15MP√a, which was already enough to startle a rapid growth rate with the 316L top layer, the crack propagation rate is observed to be close to ….. . Then at the interface transition toward the IN718 bottom layer the stress intensity factor was about MPa√m, and the propagation rate was already relatively high, however a decrease of the slope of the propagation rate is observed, getting to about …. . Thus even is the shielding effect of the propagation rate is not drastic, the effect is still visible in the reduction of the slope of the propagation rate. Additionally, Figure 15 a) show a map of the roughness of the final fracture surface of specimen N°2 showing that a very rough fracture surface can be observed in the 316L top layer, even showing a larger granular artefact clearly detached within the 316L region before the interface. While within the bottom part of the specimen, within the IN718 layer the surface remains smooth and propagation shows a homogeneously flat surface, ever with higher values of stress intensity factor. Which reveals a homogeneous propagation resistance after the interface transition.

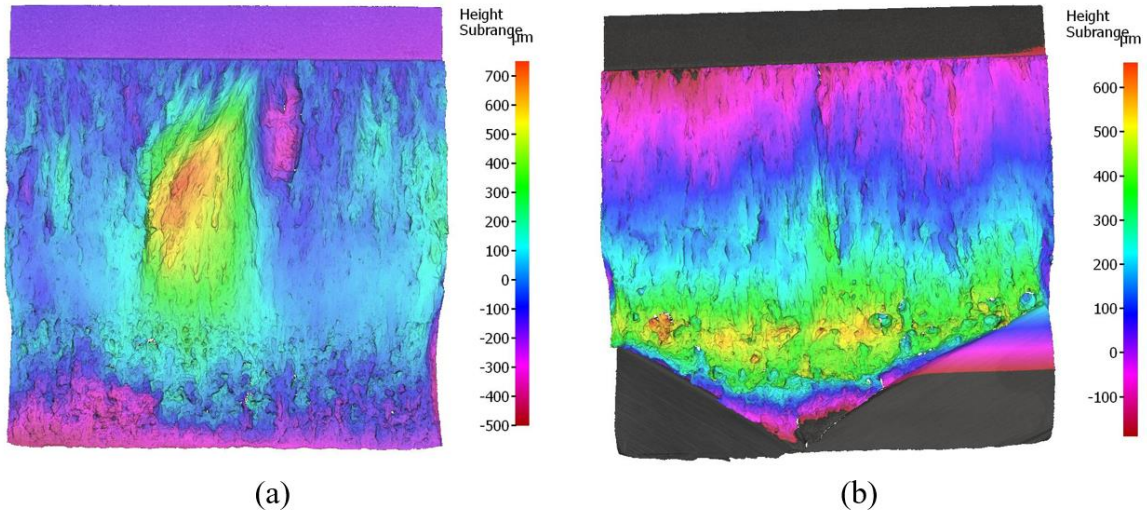

Figure 15: Roughness map of fracture surfaces, long crack test with increasing ΔK in HTed bi layer specimen, a) propagation from 316L top layer to IN718 bottom layer (specimen N°2), b) from 316L top layer to IN718 bottom layer (specimen N°1)

It can be conclude from these tests that the crack propagation measured in both specimen for the IN718 layer is resistant and display a good reduction of propagation rate, while for the 316L layer in both specimen the propagation rate seems to have been increased, hence reduce its resistance to propagation. And even in shielding and anti-shielding mechanisms were observed, the effect of these mechanisms seems to be less impactful then the intrinsic crack propagation resistance of each separated material microstructure. It appears that the microstructure strength has a major effect on the crack propagation resistance, that the heat treatment has improved the mechanical response of IN718, while diminishing the response of 316L alloy. The geometrical aspect of the thickness of each layer also impacts the stress intensity factor, as the crack propagation progresses. Meaning that if a shielding effect can be positive, the anti-shielding effect can be detrimental further more if the depth of the crack tip reaches this type of transition at an already elevated value, meaning that if the design can be made the anti-shielding type of interface should be located closer to the start of crack propagation while the stress intensity factor is still low in order to limit its impact. Similarly if the anti-shielding is used in a design to support the mitigation of crack propagation, it should be supported by a strong microstructure, hence the heat treatment of IN718 has shown positive impact on its crack propagation resistance and is expected to play a major role in the crack propagation resistance in both of our the tests.

3.4.2 Bilayer specimen fractography

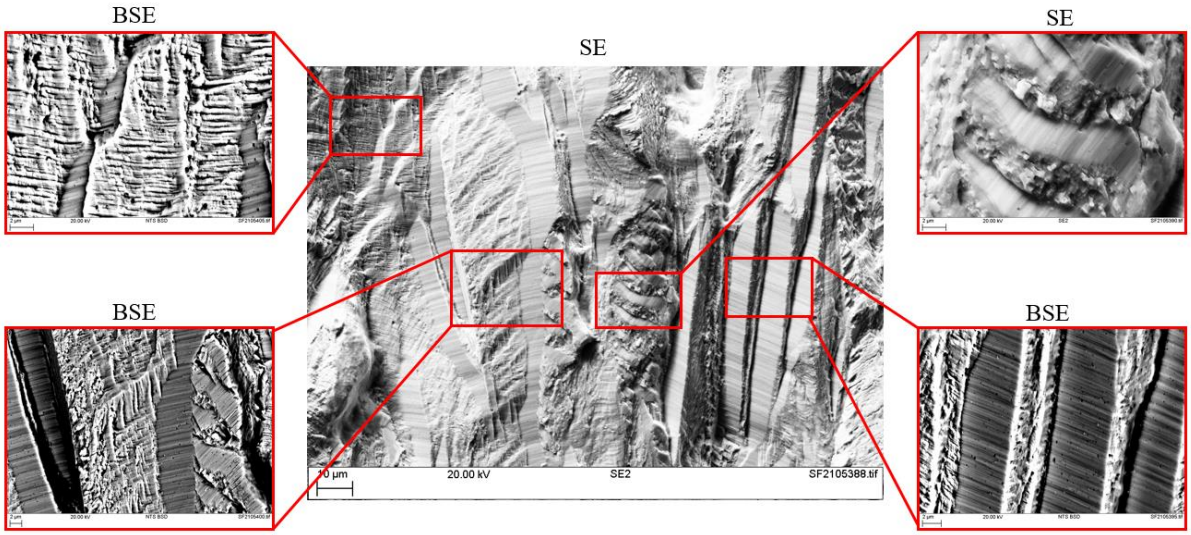

Figure 16: SEM view of specimen N°1 fracture surface, magnified within 316L bottom layer, view in BSE and SE of magnified areas

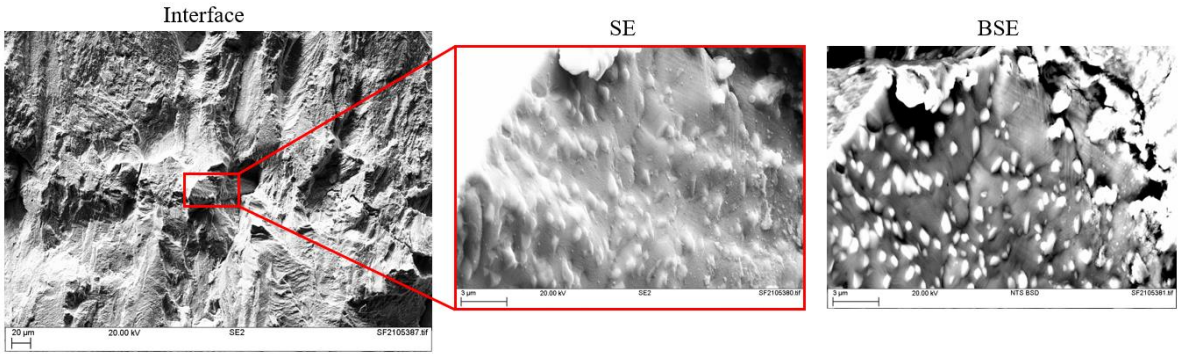

Figure 17: SEM image of the Interface of specimen N°1, SE and BSE magnified view of intermetallic phases

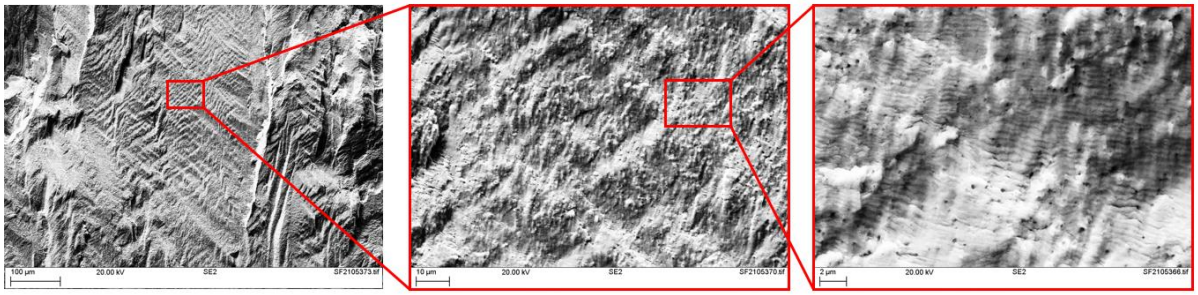

Figure 18: SEM view of specimen N°1 fracture surface, magnified within 316L bottom layer

Figure 16, Figure 17 and Figure 18 show SEM images of the final fracture surface of specimen N°1.

Figure 16 shows magnified areas of the top IN718 layer where crack propagation was reported to be reduced, and it can be seen elongated flat areas adjacent to step-like regions. Under Backscatter imaging (BSE) small spherical secondary phases were observed throughout the surface with no apparent effect on the crack propagation. It can be understand that a majority of intragranular propagation has taken place along the elongated columnar grains, and that the

resistance of crack propagation is mostly due to grain strengthening with no apparent impairment of detrimental secondary phases.

Figure 17 shows a magnified view of the interface microstructure and clear secondary phases where observed under BSE imaging, which is coherent with previous observation of the HTed microstructure (see section 3.2). Some secondary crack where observed along the grain boundaries but in the interface region, but no major decohesion around the intermetallic phases were observed.

Figure 18 shows a magnified view of the 316L bottom layer of specimen N°1, where wavy type of features were supper imposed on the globular macro-dimple features of the surface. The striations were measured to be ~ 0.4 µm at about 5.715 mm depth which is coherent with the propagation rate displayed in Figure 14 for a ΔK of 30MPa√m.

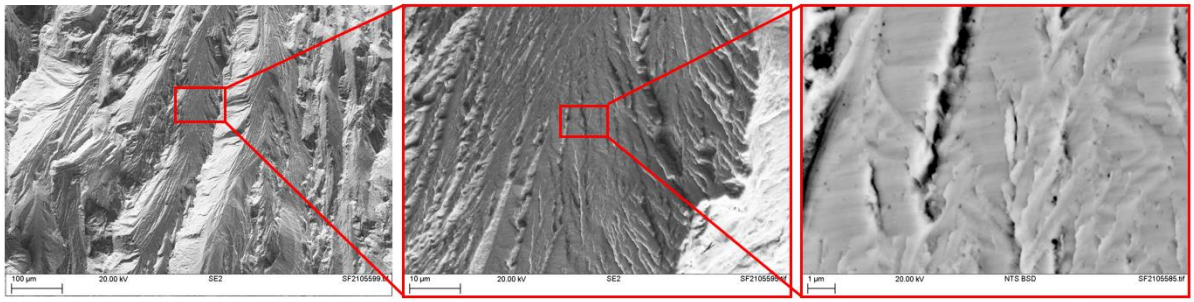

Figure 19: SEM view of specimen N°2 fracture surface, magnified within 316L top layer

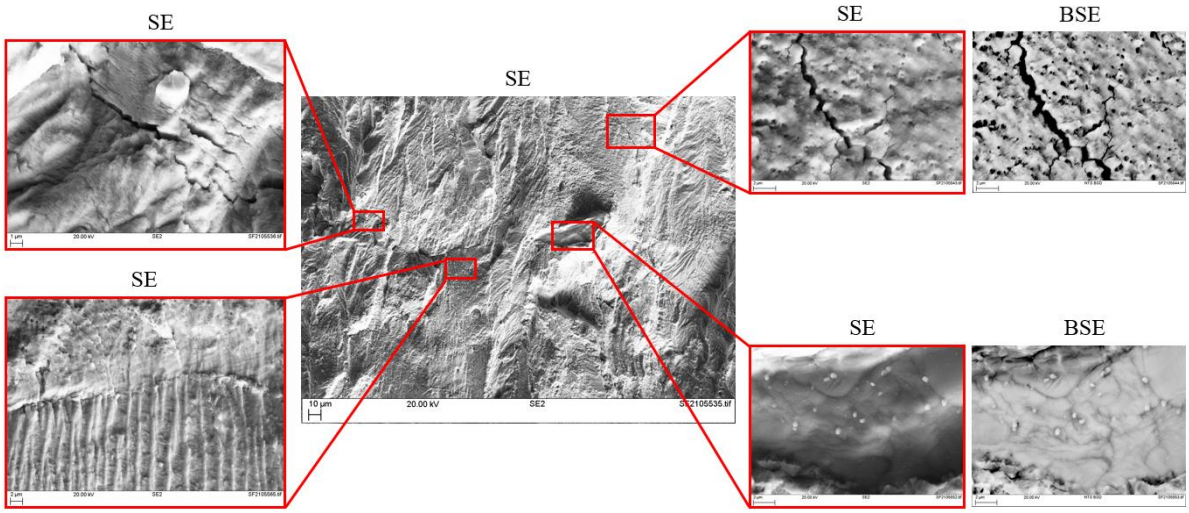

Figure 20: SEM view of specimen N°2 fracture surface, magnified view of the interface in SE and BSE

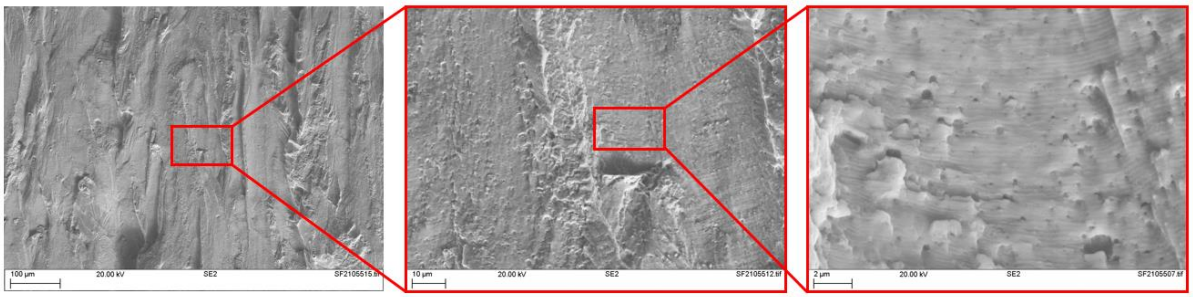

Figure 21: SEM view of specimen N°2 fracture surface, magnified within IN718 bottom layer

Figure 19 , Figure 20 and Figure 21 show SEM images of the final fracture surface of specimen N°2.

Figure 19 shows magnified areas of the top 316L layer where the crack propagation rate was consistently increasing at a rapid rate and showing rough macroscopic features on the surface. Coarse slip bands were observed under SEM magnified view both intragranular and intergranular.

Figure 20 shows a magnified view of the microstructure around the interface. Secondary crack were observed within the 316L layer around the interface area, and were observed to connect secondary phases. Secondary phase were also observed within the internal surface of a porosity, and clearly observed under BSE magnified view.

Figure 21 shows a magnified view of the IN718 bottom layer of specimen N°2, long intragranular flat crack propagation can be observed. The striations were measured to be ~ 0.21 µm at about 5.7 mm depth which is coherent with the propagation rate displayed in Figure 14 for a ΔK of 35MPa$\sqrt{m}$.

It can be conclude from these observations that the shielding effect is mainly acting as opening of a network of secondary cracks connecting intermetallic secondary phases within the 316L layer just before the interface transition. The propagation of crack in IN718 seems to be intragranular thus the propagation resistance is supposed to be supported by intrinsic microstructure strength. Whereas the crack propagation rate within the 316L layers seems to have been increased after HT due to a reduction of microstructural strength. However, neither any detrimental interaction between secondary phases nor the matrix were observed, nor any decohesion around the interface were observed. Which supports the conclusion that the relative effect of interface transition on crack propagation rate mitigation remains less impacting than each alloy respective mechanical strength.

3.4.3 4-layer specimen

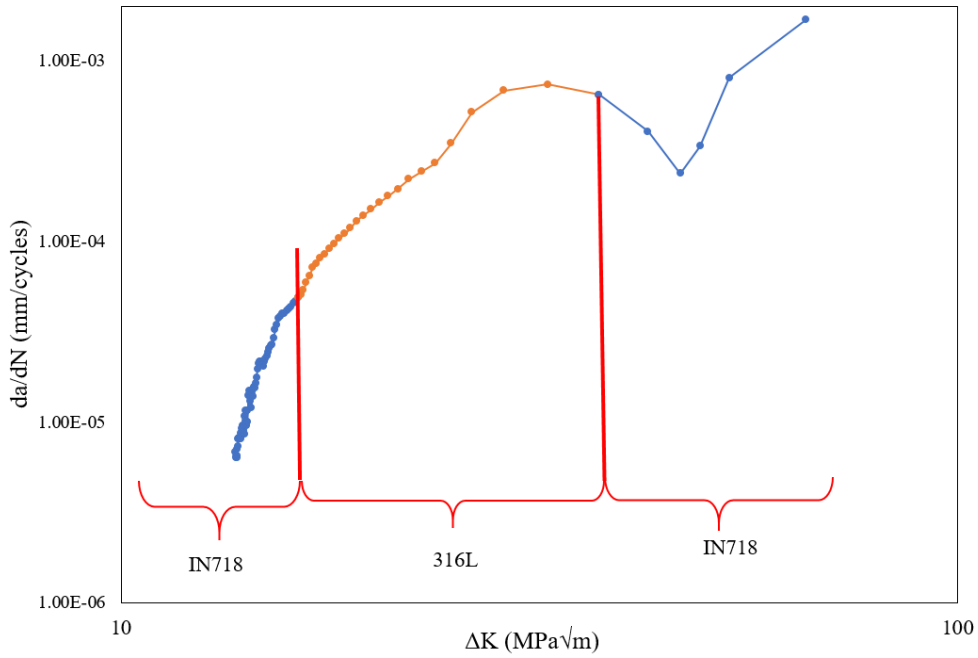

Figure 22 Long crack test with increasing ΔK through 4-layers specimen in HTed condition

3.4.4 4-layer specimen fractography

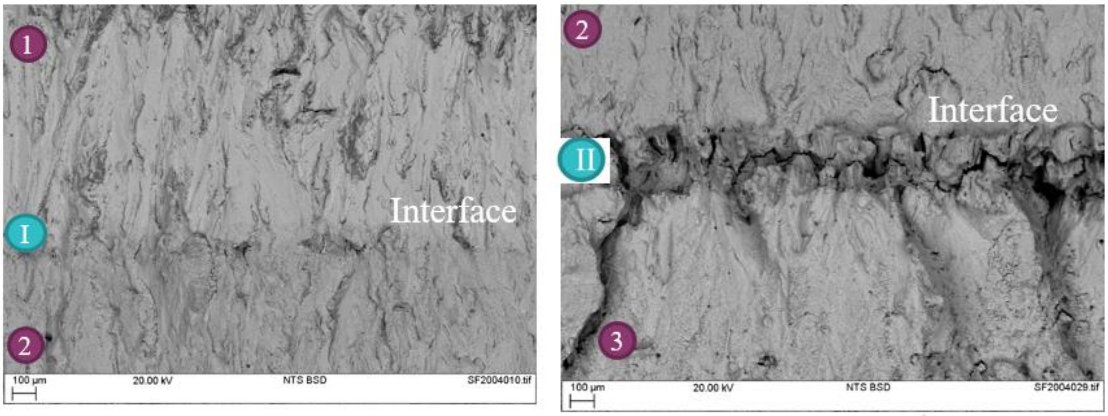

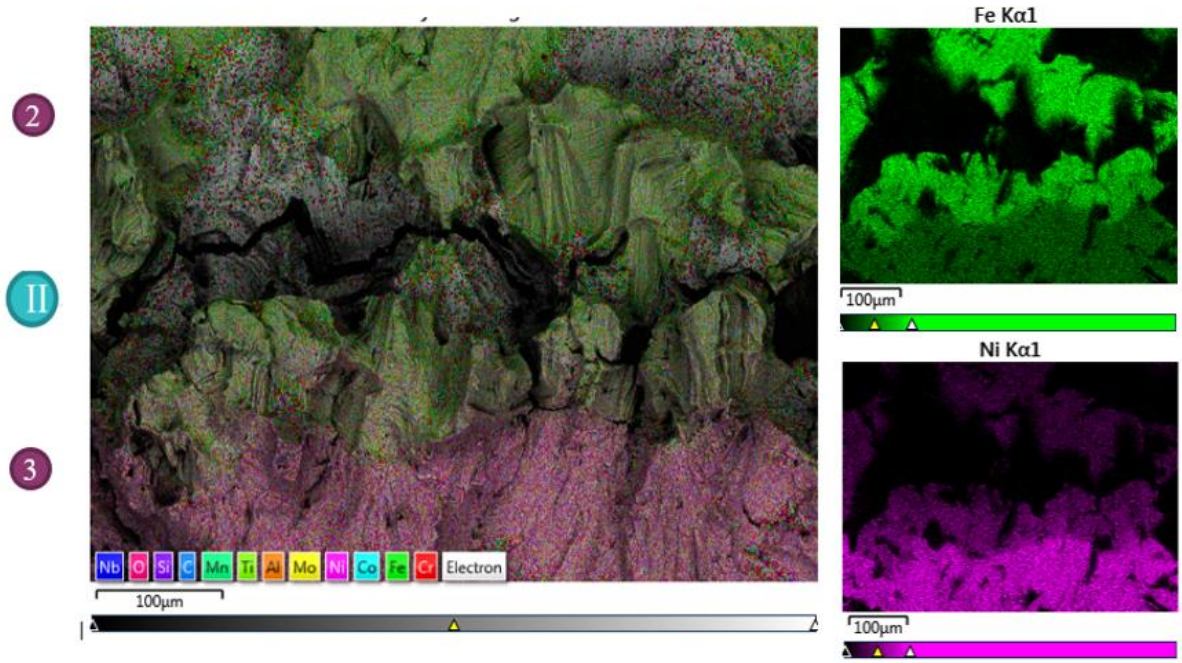

4. Conclusions

5. References

[1] A. Busachi, J. Erkoyuncu, P. Colegrove, F. Martina, C. Watts, and R. Drake, "A review of Additive Manufacturing technology and Cost Estimation techniques for the defence sector," *CIRP J. Manuf. Sci. Technol.*, vol. 19, pp. 117–128, 2017.

[2] M. Vaezi, S. Chianrabutra, B. Mellor, and S. Yang, "Multiple material additive manufacturing - Part 1: A review: This review paper covers a decade of research on multiple material additive manufacturing technologies which can produce complex geometry parts with different materials," *Virtual Phys. Prototyp.*, vol. 8, no. 1, pp. 19–50, 2013.

[3] M. Naebe and K. Shirvanimoghaddam, "Functionally graded materials: A review of fabrication and properties," *Appl. Mater. Today*, vol. 5, pp. 223–245, 2016.

[4] B. E. Carroll *et al.*, "Acta Materialia Functionally graded material of 304L stainless steel and inconel 625 fabricated by directed energy deposition : Characterization and thermodynamic modeling," *Acta Mater.*, vol. 108, pp. 46–54, 2016.

[5] A. Hinojos *et al.*, "Joining of Inconel 718 and 316 Stainless Steel using electron beam melting additive manufacturing technology," *Mater. Des.*, vol. 94, pp. 17–27, 2016.

[6] O. Kolednik, "The yield stress gradient e ect in inhomogeneous materials," *Int. J. solids Struct. 37*, vol. 37, pp. 781–808, 2000.

[7] S. Mohd Yusuf, M. Nie, Y. Chen, S. Yang, and N. Gao, "Microstructure and corrosion performance of 316L stainless steel fabricated by Selective Laser Melting and processed through high-pressure torsion," *J. Alloys Compd.*, vol. 763, pp. 360–375, 2018.

[8] E. Chlebus, K. Gruber, B. Ku, J. Kurzac, and T. Kurzynowski, "Materials Science & Engineering A Effect of heat treatment on the microstructure and mechanical prop- erties of Inconel 718 processed by selective laser melting," vol. 639, pp. 647–655, 2015.

[9] I. Tolosa, F. Garciandía, F. Zubiri, F. Zapirain, and A. Esnaola, "Study of mechanical properties of AISI 316 stainless steel processed by 'selective laser melting', following different manufacturing strategies," *Int. J. Adv. Manuf. Technol.*, vol. 51, no. 5–8, pp. 639–647, 2010.

[10] T. Trosch, J. Strößner, R. Völkl, and U. Glatzel, "Microstructure and mechanical properties of selective laser melted Inconel 718 compared to forging and casting," *Mater. Lett.*, vol. 164, pp. 428–431, 2016.

[11] S. J. Zinkle and G. S. Was, "Materials challenges in nuclear energy," *Acta Mater.*, vol. 61, no. 3, pp. 735–758, 2013.

[12] C. Wei and E. T. Al, "Multiple-Material selective laser melting : a new approach :," *laser user*, no. 89, pp. 18–19, 2018.

[13] J. F. Radavich, "THE PHYSICAL METALLURGY OF CAST AND WROUGHT ALLOY 718 Cast Alloy 718," 1989.

[14] C. Kuo, Y. Yang, H. Bor, C. Wei, and C. Tai, "Aging effects on the microstructure and creep behavior of Inconel 718 superalloy," vol. 511, pp. 289–294, 2009.

[15] M. Calandri *et al.*, "Solution Treatment Study of Inconel 718 Produced by SLM Additive Technique in View of the Oxidation Resistance," vol. 1800351, pp. 1–16, 2018.

[16] P. Petrzak, K. Kowalski, and M. Blicharski, "Analysis of Phase Transformations in Inconel 625 Alloy during Annealing," *Acta Phys. Pol. A*, vol. 130, no. 4, 2016.

[17] W. M. Tucho, P. Cuvillier, A. Sjolyst-kverneland, and V. Hansen, "Materials Science & Engineering A Microstructure and hardness studies of Inconel 718 manufactured by selective laser melting before and after solution heat treatment," *Mater. Sci. Eng. A*, vol. 689, no. February, pp. 220–232, 2017.

[18] X. Li *et al.*, "Effect of heat treatment on microstructure evolution of Inconel 718 alloy fabricated by

selective laser melting," vol. 764, 2018.

[19] O. M. D. M. Messé, R. Muñoz-moreno, T. Illston, S. Baker, and H. J. Stone, "Metastable carbides and their impact on recrystallisation in IN738LC processed by selective laser melting," *Addit. Manuf.*, vol. 22, no. November 2017, pp. 394–404, 2018.

[20] A. S. M. International, S. Steels, and D. Engineers, "Austenitic Stainless Steels," 2008.

[21] A. F. Padilha, "Decomposition of Austenite in Austenitic Stainless Steels," no. January, 2002.

[22] D. Deng, R. Lin, H. Brodin, and J. Moverare, "Materials Science & Engineering A Microstructure and mechanical properties of Inconel 718 produced by selective laser melting : Sample orientation dependence and e ff ects of post heat treatments," *Mater. Sci. Eng. A*, vol. 713, no. July 2017, pp. 294–306, 2018.

[23] S. Sui, J. Chen, E. Fan, H. Yang, X. Lin, and W. Huang, "Materials Science & Engineering A The in fl uence of Laves phases on the high-cycle fatigue behavior of laser additive manufactured Inconel 718," *Mater. Sci. Eng. A*, vol. 695, no. February, pp. 6–13, 2017.

[24] O. Kolednik, J. Zechner, and J. Predan, "Scripta Materialia Improvement of fatigue life by compliant and soft interlayers," *SMM*, vol. 113, pp. 1–5, 2016.

[25] W. J. Sames, F. A. List, S. Pannala, R. R. Dehoff, and S. S. Babu, "The metallurgy and processing science of metal additive manufacturing," *Int. Mater. Rev.*, vol. 61, no. 5, pp. 315–360, 2016.

[26] H. D. Carlton, A. Haboub, G. F. Gallegos, D. Y. Parkinson, and A. A. Macdowell, "Materials Science & Engineering A Damage evolution and failure mechanisms in additively manufactured stainless steel," *Mater. Sci. Eng. A*, vol. 651, pp. 406–414, 2016.

[27] D. Wang, C. Song, Y. Yang, and Y. Bai, "Investigation of crystal growth mechanism during selective laser melting and mechanical property characterization of 316L stainless steel parts," *Mater. Des.*, vol. 100, pp. 291–299, 2016.

[28] Y. M. Wang *et al.*, "Additively manufactured hierarchical stainless steels with high strength and ductility," *Nat. Mater.*, vol. 17, no. 1, pp. 63–70, 2018.

[29] Y. Zhong, L. Liu, S. Wikman, D. Cui, and Z. Shen, "Intragranular cellular segregation network structure strengthening 316L stainless steel prepared by selective laser melting," *J. Nucl. Mater.*, vol. 470, pp. 170–178, 2016.

[30] J. Suryawanshi, K. G. Prashanth, and U. Ramamurty, "Mechanical behavior of selective laser melted 316L stainless steel," *Mater. Sci. Eng. A*, vol. 696, no. April, pp. 113–121, 2017.

[31] K. Saeidi, X. Gao, Y. Zhong, and Z. J. Shen, "Hardened austenite steel with columnar sub-grain structure formed by laser melting," *Mater. Sci. Eng. A*, vol. 625, pp. 221–229, 2015.

[32] "ASTM B213-20 Standard Test Methods for Flow Rate of metal Powders Using the Hall Flowmeter Funnel," *ASTM Int.*, 2020.

[33] S. M. Yusuf and N. Gao, "Influence of energy density on metallurgy and properties in metal additive manufacturing," *Mater. Sci. Technol.*, vol. 33, no. 11, pp. 1269–1289, 2017.

[34] M. Ni, C. Chen, X. Wang, P. Wang, R. Li, and X. Zhang, "Materials Science & Engineering A Anisotropic tensile behavior of in situ precipitation strengthened Inconel 718 fabricated by additive manufacturing," *Mater. Sci. Eng. A*, vol. 701, no. June, pp. 344–351, 2017.

[35] T. Peng and C. Chen, "Influence of energy density on energy demand and porosity of 316L stainless steel fabricated by selective laser melting," *Int. J. Precis. Eng. Manuf. Technol.*, vol. 5, no. 1, pp. 55–62, 2018.

[36] BS EN ISO 6507, "Vickers hardness test.," *Stand. Test Methods Met. Mater.*, 2018.

[37] ASTM, "E8/E8M A. Standard test Methods for Tension Testing of Metallic Materials," *ASTM Int.*, vol.

16ae1.

[38] British Standard Institution, “BS ISO 12108 Metallic materials — Fatigue testing — Fatigue crack growth method,” *Int. Stand.*, 2012.

[39] AMS2759, “Heat Treatment of Steel Parts, General Requirement,” *SAE Int.*, 2019.

[40] AMS5662, “NickelAlloy, Corrosion and Heat Resistant, Bars, Forging, and Ring 52.5Ni19Cr3.0Mo5.1Cb0.9Ti0.5Al18Fe, Consumable Electrode or Vacuum Induction Melted 1775F Solution Heat Treated, Precipitation Hardenable,” *SAE Int.*

[41] AMS5383, “Nickel Alloy, Corrosion and Heat-Resistant, Investment Casting, 52.5Ni-19Cr-3.0Mo-5.1Cb(Nb)-0.9Ti-0.6Al-18Fe, Vacuum Melted Homogenization and Solution Heat Treated,” *SAE Int.*

[42] M. S. Pham, B. Dovgyy, and P. A. Hooper, “Twinning induced plasticity in austenitic stainless steel 316L made by additive manufacturing,” *Mater. Sci. Eng. A*, vol. 704, no. April, pp. 102–111, 2017.

[43] Sandmayer, “Specification Sheet : Alloy 316 / 316L,” no. 1, pp. 9–11, 2014.

[44] Special metals, “INCONEL alloy 718,” *Spec. Met.*, 2007.

[45] T. Keil, E. Bruder, and K. Durst, “Exploring the compositional parameter space of high-entropy alloys using a diffusion couple approach,” *Mater. Des.*, vol. 176, p. 107816, 2019.

[46] G. Posch, R. Vallant, W. Klagges, and H. Cerjak, “Influence of Niobium on mechanical properties and hot crack susceptibility of Nickel-base cored-wire weld metal type 70 / 20 and 70 / 15 Cracking in Nickelbasis-weldments Solidification cracking,” vol. 2000, 2000.

[47] R. R. Unocic and J. N. DuPont, “Process Efficiency Measurements in the Laser Engineered Net Shaping Process,” *Metall. Mater. Trans. B Process Metall. Mater. Process. Sci.*, vol. 35, no. 1, pp. 143–152, 2004.

[48] M.C.Flemings, “Solidification Processing,” *Metall. Trans.*, vol. 5, 1974.

[49] S. D. K. John N Dupont, John CLippold, *Welding Metallurgy and Weldalitity of Nickel-base alloys*. 2009.

[50] Z. Jones, K. Cooper, and K. Chou, “Characterisation of Microstructure and Mechanical Property of Inconel 718 from Selective Laser Melting,” *Int. mafufacturing Sci. Eng.*, no. January 2015, 2017.

[51] D. Wang, C. Song, Y. Yang, and Y. Bai, “Investigation of crystal growth mechanism during selective laser melting and mechanical property characterization of 316L stainless steel parts,” *JMADE*, vol. 100, pp. 291–299, 2016.